



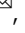


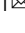


Inverse ZrO₂/Cu as a highly efficient methanol synthesis catalyst from CO₂ hydrogenation

Congyi Wu^{1,11}, Lili Lin^{1,2,3,11}, Jinjia Liu^{4,5,6,11}, Jingpeng Zhang⁷, Feng Zhang⁸, Tong Zhou⁹, Ning Rui², Siyu Yao², Yuchen Deng¹, Feng Yang¹, Wenqian Xu¹⁰, Jun Luo⁹, Yue Zhao¹, Binhang Yan⁷, Xiao-Dong Wen¹^{4,5,6}, José A. Rodríguez^{2,8}¹¹ & Ding Ma¹¹¹

Enhancing the intrinsic activity and space time yield of Cu based heterogeneous methanol synthesis catalysts through CO₂ hydrogenation is one of the major topics in CO₂ conversion into value-added liquid fuels and chemicals. Here we report inverse ZrO₂/Cu catalysts with a tunable Zr/Cu ratio have been prepared via an oxalate co-precipitation method, showing excellent performance for CO₂ hydrogenation to methanol. Under optimal condition, the catalyst composed by 10% of ZrO₂ supported over 90% of Cu exhibits the highest mass-specific methanol formation rate of 524 g_{MeOH}kg_{cat}⁻¹h⁻¹ at 220 °C, 3.3 times higher than the activity of traditional Cu/ZrO₂ catalysts (159 g_{MeOH}kg_{cat}⁻¹h⁻¹). In situ XRD-PDF, XAFS and AP-XPS structural studies reveal that the inverse ZrO₂/Cu catalysts are composed of islands of partially reduced 1-2 nm amorphous ZrO₂ supported over metallic Cu particles. The ZrO₂ islands are highly active for the CO₂ activation. Meanwhile, an intermediate of formate adsorbed on the Cu at 1350 cm⁻¹ is discovered by the in situ DRIFTS. This formate intermediate exhibits fast hydrogenation conversion to methoxy. The activation of CO₂ and hydrogenation of all the surface oxygenate intermediates are significantly accelerated over the inverse ZrO₂/Cu configuration, accounting for the excellent methanol formation activity observed.

¹Beijing National Laboratory for Molecular Sciences, College of Chemistry and Molecular Engineering and College of Engineering and BIC-ESAT Peking University, Beijing 100871, China. ²Chemistry Department, Brookhaven National Laboratory, Upton, NY 11973, USA. ³Institute of Industrial Catalysis, State Key Laboratory of Green Chemistry Synthesis Technology, College of Chemical Engineering, Zhejiang University of Technology, Hangzhou 310032, China. ⁴State Key Laboratory of Coal Conversion, Institute of Coal Chemistry, Chinese Academy of Sciences, Taiyuan, China. ⁵National Energy Centre for Coal to Liquids, Synfuels China Co. Ltd, Beijing, China. ⁶Beijing Advanced Innovation Center for Materials Genome Engineering, Industry-University Cooperation Base between Beijing Information S&T University and Synfuels China Co. Ltd, Beijing, China. ⁷Department of Chemical Engineering, Tsinghua University, Beijing 100084, China. ⁸Materials Science and Chemical Engineering Department, State University of New York at Stony Brook, New York, NY 11794, United States. ⁹Center for Electron Microscopy, Tianjin University of Technology, Tianjin 300384, China. ¹⁰X-ray Science Division, Advanced Photon Source, Argonne National Laboratory, Argonne, Lemont, IL 60439, USA. ¹¹These authors contributed equally: Congyi Wu, Lili Lin, Jinjia Liu. ✉email: linll@zjut.edu.cn; wxd@sxicc.ac.cn; rodriguez@bnl.gov; dma@pku.edu.cn

An increase of CO₂ emissions caused by the extreme utilization of fossil fuels has led to serious concerns upon the crisis of global warming, the rising of ocean levels and sea acidification^{1–3}. One of the most promising ways to mitigate the negative effects of excessive CO₂ emissions is to convert the pollutant back into value-added chemicals and fuels, achieving a carbon neutral system by utilizing the CO₂ as a carbon source^{4–6}. The methanol economy⁷, advocated by George A. Olah⁸, proposes that the use of methanol or dimethyl ether can probably replace fossil fuels in the energy storage and ground transportation in the future^{9–11}. Recent development of more efficient catalysts for the methanol to olefin/gasoline (MTO and MTG) reactions has also made the methanol a potential key compound for the manufacture of bulk chemicals^{12,13}. Therefore, intensive research and effort have been devoted to finding high-performance catalysts for CO₂ hydrogenation to methanol which may not have standard metal-oxide configurations or the typical copper and zinc oxide components of commercial catalysts^{14–17}.

Copper-based catalysts have been widely investigated in the synthesis of methanol through CO₂ hydrogenation^{17–19}. In previous studies, it has been shown that Cu/ZrO₂ systems exhibited promising catalytic performance²⁰. Compared with other oxide supports, zirconia has been proven to be superior in promoting the catalytic performances of Cu-based catalysts in methanol synthesis through CO₂ hydrogenation, especially due to its capability of inhibiting byproducts such as CO and methane²¹. Structural and mechanistic investigations suggested that the Cu-ZrO₂ interface played a vital role in the selective formation of methanol, which facilitate the formation, further hydrogenation and desorption of the active surface intermediates^{22–25}. To maximize the Cu-ZrO₂ interface, it has been reported that amorphous ZrO₂ was able to accommodate Cu in its lattice exhibiting much better performances than the crystalline tetragonal ZrO₂ and monoclinic ZrO₂ references^{26,27}. Theoretical calculations even suggested that ZrO₂ did not need to be presented as a bulk material in the catalyst²¹. In a study, isolated ZrO_x motifs dispersed on high surface area silica were able to promote the methanol synthesis activity and selectivity of supported Cu domains²⁸.

These findings motivated us to investigate the CO₂ hydrogenation over catalysts with a ZrO₂/Cu inverse configuration in which the domains of zirconia only covered a small fraction of the metallic copper surface. At small coverages of zirconia, one can expect special structural and electronic properties not seen in the bulk material plus strong oxide↔copper interactions. Although being rarely investigated in powder catalysts, the inverse oxide/metal configuration has been shown to enhance interfacial reactivity in well-defined CeO_x/Cu(111) and ZnO/Cu(111) model surfaces^{29,30} used as catalysts for the water-gas shift and methanol synthesis reactions. Furthermore, a ZnO/Cu configuration has been proposed as the actual active phase in a Cu/ZnO/Al₂O₃ powder catalyst³¹. In principle, an optimization of the oxide component in such an inverse oxide/metal configuration could lead to a better activity and selectivity for methanol synthesis^{32,33}. Here, we move away from ZnO and work with a multivalent oxide component. In this article, combining catalytic tests and in-situ characterization, we show that ZrO₂/Cu catalysts exhibit excellent performance in methanol synthesis, validating the idea of using inverse oxide/copper configurations aiming at a rational design of efficient catalysts for the CO₂ to CH₃OH conversion.

Results

The structural characterization of the ZrO₂/Cu catalysts. A series of catalysts with a ZrO₂/Cu-*x* composition (where *x* is the weight percentage of ZrO₂ in the sample and had values of 0.05,

0.1, 0.2, 0.5, and 0.9) were synthesized by using an oxalate coprecipitation (CP) method (for details of this approach see corresponding text in Methods and Supplementary Table 1)³⁴. The powder diffraction profiles of the synthesized catalysts after calcination are shown in Fig. 1a. As no crystalline zirconia phases has been observed in any of the ZrO₂/Cu-*x* catalysts, it was clear that the obtained ZrO₂ species through the oxalate CP method were probably in an amorphous state. Zr K edge X-ray adsorption fine structure (XAFS) spectroscopy was collected to identify the local structure of the well dispersed ZrO₂ nanoparticles. Since the Zr K edge FT-EXAFS spectra of both the ZrO₂/Cu-0.1 and the ZrO₂/Cu-0.9 catalysts showed similar R space structure with very small intensities of the second nearest neighbor Zr–Zr coordination, it is likely that the zirconia domains in the different ZrO₂ loading catalysts have a similar geometrical structure (Fig. 1b). The pair distribution function (PDF) of the total x-ray diffraction of the amorphous ZrO₂/Cu-0.9 catalyst was also collected to understand the structure of ZrO₂ particles in the Zr rich catalyst (Fig. 1c). Based on the PDF profile, the nearest Zr–O pair distance is 2.13 Å and the nearest Zr–O–Zr pair appeared at 3.42 Å³⁵, which correlates well with the Zr K edge EXAFS fitting results (Supplementary Fig. 1, Supplementary Table 2). The intensity of the oscillation of the PDF profile damped very quickly, and disappeared at ~12 Å, indicating that most of the ZrO₂ particles had a size around 1.2 nm. When NaOH was used as the precipitating substance, the diffraction patterns of the ZrO₂ could be observed for the resulted ZrO₂/Cu-0.9-NaOH catalyst (Supplementary Fig. S2), indicating that the oxalate CP method tends to generate zirconia domains with a small size and amorphous structure, which is different from the traditional NaOH precipitation method. The structural information for the ZrO₂/Cu-0.1 catalyst and ZrO₂/Cu-0.9 catalyst was further confirmed by high-resolution scanning transmission electron microscopy (HR-STEM) and energy dispersive spectroscopy (EDS)-elemental mapping images (Fig. 1d–g). The local fast Fourier Transformation (FFT)³⁶ derived from the high-angle annular dark field (HAADF)-STEM images suggested that the CuO in the ZrO₂/Cu-0.1 catalyst consist of monoclinic crystals (ICSD 69094, space group: C 1 2/c 1) oriented along the [01̄1] direction (Fig. 1d). However, the ZrO₂ was present as amorphous species which decorated the surface of the CuO particles (around 15–20 nm), as no lattice fringes of ZrO₂ could be resolved in the STEM images. The EDS elemental mapping images in Fig. 1e demonstrate that the ZrO₂ component is highly dispersed on the CuO substrate. The decreasing percentage of Cu in the catalysts results in the transformation of Cu species from large particles (ZrO₂/Cu-0.1, around 15–20 nm) to small particles (ZrO₂/Cu-0.9, around 1–2 nm, Fig. 1f–g), which is in good agreement with the X-ray diffraction (XRD) patterns (Fig. 1a). Based on the characterizations, ZrO₂/Cu-0.1 catalyst is named as inverse catalysts as the Cu becomes the major component as a support in the catalyst. The term “inverse catalyst” is an analogue of the previous studies in the surface science research³⁰, which describes the catalyst composed by oxide islands that only covered a small part of the metal surfaces. When the ZrO₂ is the dominant component, such as the ZrO₂/Cu-0.9 system, the catalyst will be recognized as conventional Cu/ZrO₂-0.1 catalysts.

Catalytic performance of ZrO₂/Cu-*x* in CO₂ hydrogenation.

The catalytic activities of the ZrO₂/Cu-*x* catalysts for methanol synthesis from CO₂ hydrogenation were evaluated at 220 °C using a gas feed of CO₂/H₂ mixture with a 1/3 ratio at 3.0 MPa. Prior to the reaction, the pristine ZrO₂/Cu-*x* catalysts were reduced by 5% H₂ at 300 °C for 2 h. During the catalytic reaction, the CO₂ conversion of the catalysts was kept below 5%, far away from the equilibrium

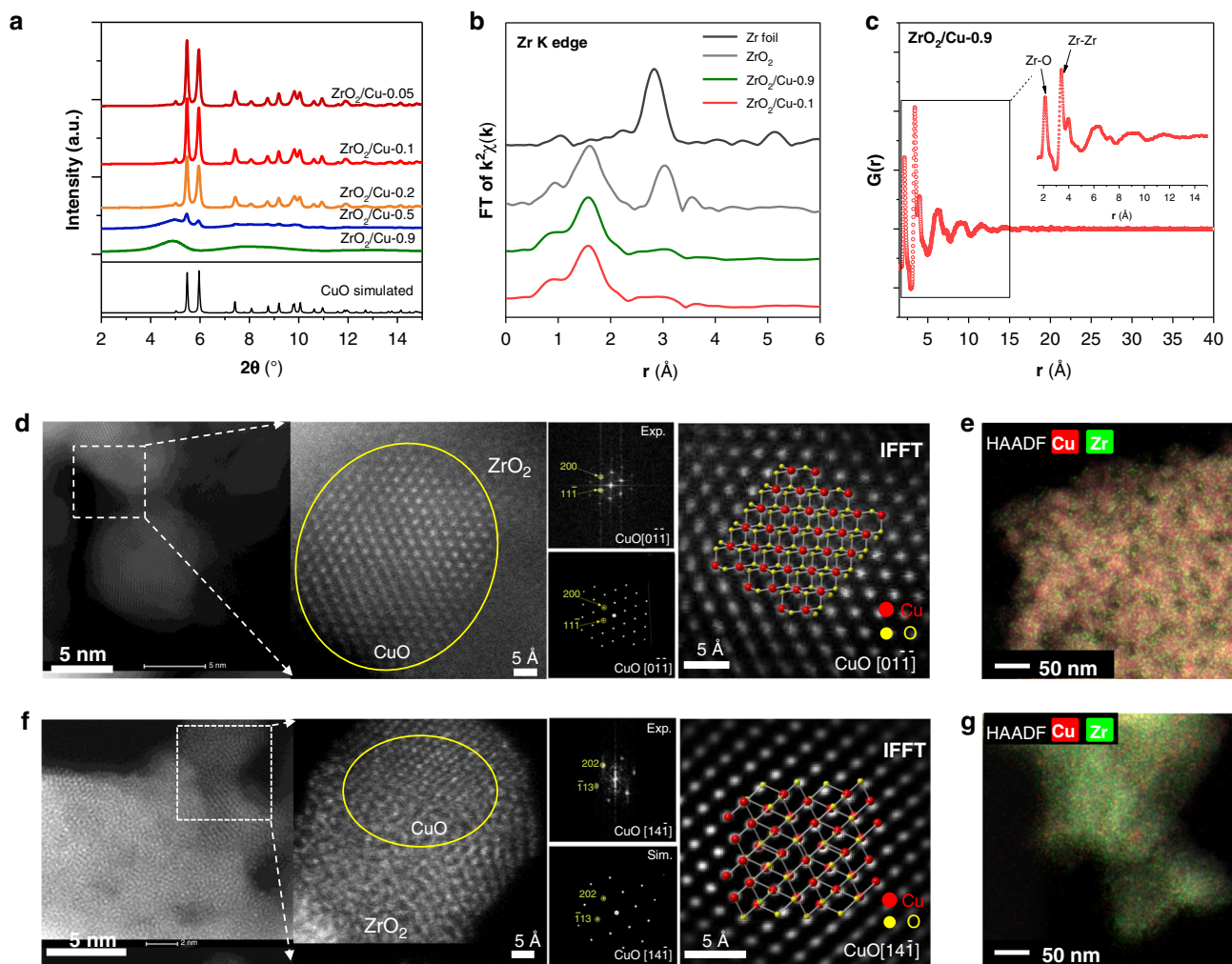


Fig. 1 Structure characterization of the $\text{ZrO}_2/\text{Cu}-x$ catalysts. **a** XRD patterns of the calcined $\text{ZrO}_2/\text{Cu}-0.05$ (dark red), $\text{ZrO}_2/\text{Cu}-0.1$ (red), $\text{ZrO}_2/\text{Cu}-0.2$ (orange), $\text{ZrO}_2/\text{Cu}-0.5$ (blue) and $\text{ZrO}_2/\text{Cu}-0.9$ (green) catalysts (wavelength of the incident X-ray, $\lambda = 0.24125 \text{ \AA}$). **b** EXAFS profiles of Zr K edge of $\text{ZrO}_2/\text{Cu}-0.1$ (red) and $\text{ZrO}_2/\text{Cu}-0.9$ (green) catalysts with Zr foil (black) and ZrO_2 standards (gray) as references. **c** PDF structural analysis of the calcined $\text{ZrO}_2/\text{Cu}-0.9$ catalyst. High-resolution HAADF-STEM images/FFT patterns with simulated results and the EDS elemental mapping of the $\text{ZrO}_2/\text{Cu}-0.1$ **d**, **e** and $\text{ZrO}_2/\text{Cu}-0.9$ **f**, **g** catalysts, respectively. The atomic structures of CuO $[0\bar{1}1]$ and $[14\bar{1}]$ are superimposed on the inverted FFT (IFFT) images. The scale bar in the **e** and **g** are 50 nm. In elementary mapping images, Zr and Cu are in green and red, respectively.

concentration of methanol (19.4%, Supplementary Fig. 3) in order to approach the intrinsic activity. Among all the catalysts with different Zr/Cu ratio, the inverse $\text{ZrO}_2/\text{Cu}-0.1$ catalyst showed the highest space time yield (STY) of methanol at a rate of $524 \text{ g}_{\text{MeOH}}/\text{kg}_{\text{cat}}^{-1}\text{h}^{-1}$, 3.3 times higher than that of the $\text{ZrO}_2/\text{Cu}-0.9$ ($\text{Cu}/\text{ZrO}_2=0.1$) catalyst ($159 \text{ g}_{\text{MeOH}}/\text{kg}_{\text{cat}}^{-1}\text{h}^{-1}$) (Fig. 2). From this $\text{ZrO}_2/\text{Cu}-0.1$ composition, the increasing or decreasing of the ZrO_2 loading both triggered a reduction in the methanol formation rate, making the rate-to- ZrO_2 loading relationship exhibit a volcano-like profile as shown in Fig. 2. What is more, the superior catalytic performance of $\text{ZrO}_2/\text{Cu}-0.1$ is also comparable to that of a commercial Topsoe catalyst, which is well-known as one of the best methanol synthesis catalyst (Supplementary Fig. 4). Therefore, it can be concluded that the combination of the amorphous ZrO_2 and Cu with a suitable Zr/Cu ratio is crucial for the construction of an excellent inverse catalyst for methanol synthesis from CO_2 . In the rest of the paper, the term of $\text{Cu}/\text{ZrO}_2-0.1$ is used as the reference of traditional catalyst.

Structural understandings of the working catalysts. To distinguish the structure characteristics of the inverse $\text{ZrO}_2/\text{Cu}-$

0.1 catalyst and traditional $\text{Cu}/\text{ZrO}_2-0.1$ catalyst which induced the different catalytic performances in CO_2 hydrogenation, we performed systematic in situ characterizations on both the inverse and conventional catalysts (Fig. 3). An in situ XRD-PDF study was carried out to investigate the crystal structure of the $\text{ZrO}_2/\text{Cu}-0.1$ catalyst under reduction and working reaction conditions of 3.0 MPa. Based on the profiles of synchrotron PDF (Fig. 3a), it could be confirmed that only the diffraction pattern of the CuO support was observable in the fresh sample. The reduction of the copper oxides into metallic copper took place at $\sim 120 \text{ }^\circ\text{C}$ (Supplementary Fig. 5). During the 2 h reaction ($220 \text{ }^\circ\text{C}$), the intensity of crystalline Cu remained intact and no peak related with Cu_2O was observed. According to the PDF fitting analysis, the Cu-Cu bond lengths are similar to those in bulk materials. Thus, no significant bond extension or contraction was observed during the reaction compared to the reduced sample (Fig. 3b), indicating that the structure of the Cu particles was stable under CO_2 hydrogenation reaction conditions. In addition, the HR-TEM image and EELS element mapping of the spent $\text{ZrO}_2/\text{Cu}-0.1$ catalyst (Supplementary Fig. 6) also demonstrate the ZrO_2 remains as highly dispersed particles loaded on large Cu. No sintering or aggregation of zirconia has been resolved. As the

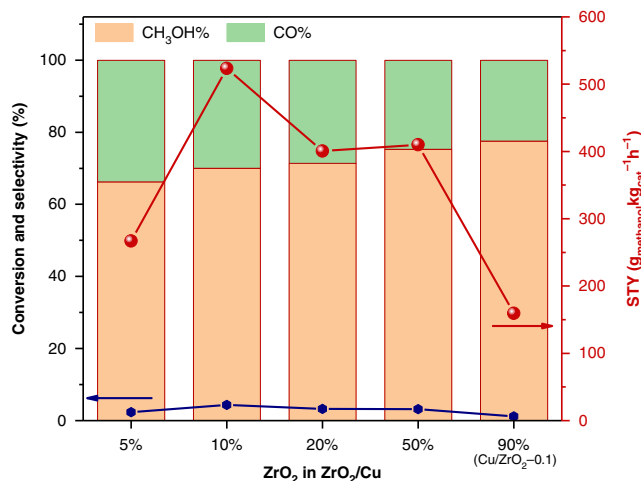


Fig. 2 The catalytic performance of ZrO₂/Cu catalysts. CO₂ conversion (blue dotted line), product selectivity (methanol: orange bar, CO: green bar) and space time yield (STY) of methanol (red dotted line) as a function of the percentage of ZrO₂ in the ZrO₂/Cu catalysts. Reaction conditions for the catalytic test: WHSV = 48,000 mL g⁻¹ h⁻¹, T = 220 °C, CO₂:H₂ = 1:3, P = 3.0 MPa. All the performance data were collected at a CO₂ conversion below 5%.

surface composition of the catalyst under reaction environment is pivotal for chemical transformations, ambient pressure X-ray photoelectron spectroscopy (AP-XPS) was employed to determine the oxidation state of Zr in the inverse ZrO₂/Cu-0.1 and traditional Cu/ZrO₂-0.1 catalysts at elevated temperatures in the presence of H₂ alone and CO₂/H₂ mixtures. As shown in Fig. 3c, the amorphous ZrO₂ species loaded on Cu were partially reduced after 2 h exposure to H₂ at 300 °C, with the binding energy of Zr 3d shifted to 182.1 eV, 0.2 eV lower than that of the fresh sample³⁷. In contrast, no shift of the Zr 3d binding energy in the Cu/ZrO₂-0.1 catalyst was observed, indicating that the reduction of ZrO₂ species on the traditional catalyst was negligible (Fig. 3d). This phenomenon indicates that the highly dispersed ZrO₂ domains over the Cu particles contain significant amount of O defects that can be formed in a reductive atmosphere (ZrO₂/Cu-0.1). The oxygen vacancies probably serve as the active sites for CO₂ capture and activation¹⁷.

DRIFTS studies on the mechanism of CO₂ hydrogenation. To elucidate the structural influences of the Cu-Zr composites on the surface adsorbates and intermediates was essential to the reaction mechanism, *operando* diffuse reflectance Fourier transform infrared spectroscopy (DRIFTS) studies were carried out under the typical CO₂ hydrogenation atmosphere (Fig. 4, Supplementary Fig. 7). The ZrO₂/Cu-0.2 was chosen as the model of the inverse catalyst instead of the ZrO₂/Cu-0.1 catalyst, because the reflectance of ZrO₂/Cu-0.1 catalyst is insufficient for performing IR measurements. As the reaction behavior of the ZrO₂/Cu-0.2 is similar with that of ZrO₂/Cu-0.1 catalyst, the IR studies will not be affected significantly. The vibration peak assignment for the major surface species is listed in Supplementary Table 3. The peaks located at 2970 and 2875, 1384 cm⁻¹ are identified as the typical features of the adsorbed formate (H-COO*), while the bands centered at 1587 and 1368 cm⁻¹ are attributed to the O-C-O vibration (denoted as C=O) of the formate species^{16,21}. The IR bands of the methoxy groups (H₃-CO*) are found at 2926, 2821 and 1147 cm⁻¹¹⁶. Based on the DRIFTS spectra under steady state at 220 °C, the vibration peaks related with formate are generally very weak compared with the carbonates and

methoxy species on the inverse ZrO₂/Cu-0.2 catalyst (Fig. 4a), indicating the formate is a relatively active intermediate on the inverse catalyst. In contrast, it was obvious that there were intense signals of two major surface species, formate and methoxy, observed over the traditional Cu/ZrO₂-0.1 catalyst (Fig. 4c). When tracking the intensity changes in the IR signals (2877, 2821 (1147) and ~1582 cm⁻¹) which belong to the representative intermediates (formate, methoxy and C=O vibrations of formate and bidentate carbonates³⁸) approaching the steady state after the catalysts were exposed to the reaction atmosphere (Fig. 4b, d, the left panel)^{21,39}, the conversion of carbonates and formates into surface methoxy is much faster over the inverse ZrO₂/Cu-0.2 catalyst. The intensity of the methoxy C-O vibration peaks at 1147 cm⁻¹ approached the steady state within only 40 min after the exposure to the reactive atmosphere (Fig. 4b, left panel). In comparison, the carbonate, formate and the methoxy species reached steady state sequentially over the traditional Cu/ZrO₂-0.1 (Fig. 4d). The methoxy intermediate reached the maximum by the end of 90 min, indicating that the hydrogenation of surface carbonates/formates into methoxy is a relatively slow step (Fig. 4d, left panel) over the conventional Cu/ZrO₂-0.1 catalyst. The CO₂ in the feed was cut off after the system reached steady state to observe the consumption of the surface species in pure H₂³⁸. The consumption of carbonates and formate species on the inverse ZrO₂/Cu-0.2 catalyst is fast. Even under such a condition, the accumulation of methoxy is weak (less than 1.2 times of the equilibrium) and the remaining methoxy intermediate on the catalyst surface by the end of the 90 min test is only 40% of its original intensity (Fig. 4b, right panel), indicating the further reductive removal of methoxy is also a quick step on the inverse catalyst. On the contrary, on the traditional Cu/ZrO₂-0.1 catalyst, with the intensity of carbonates and formate dropping (see Fig. 4d, right panel), the methoxy accumulated and its intensity reached 1.4 time higher than the equilibrium intensity before it was gradually consumed (the final intensity still above the initial value after 90 min reaction) (Supplementary Fig. 8). This phenomenon suggested that the hydrogenation of methoxy to methanol is kinetically even slower than the conversion of carbonates and formate to methoxy. Noticeably, except for the commonly appeared IR bands, a peak at 1350 cm⁻¹ (HCOO-Cu)⁴⁰ appeared on the inverse catalyst, which hardly appeared on the traditional catalyst (Fig. 4e, Supplementary Fig. 9). Based on the literature, the new band is attributed to the O-C-O vibration of the formatted species bonded on Cu or the interface, which is about 18 cm⁻¹ lower than those adsorbed on the ZrO₂ (bidentate formate⁴¹). The generation and consumption of HCOO-Cu were extremely fast under transient condition compared with the formate species on zirconia, which demonstrates a highly reactive reaction pathways existed on the inverse catalyst (Fig. 4b). The adsorption site of this intermediate, the metallic Cu, facilitates the hydrogenation conversion of the formate and enhances the turnover frequencies (TOF) of the oxygenates on the inverse catalysts. Summarizing the information of the in situ DRIFTS results, it could be deduced that the reason of the superior performance of the inverse configuration with optimized Zr/Cu ratio is that the oxygenate intermediates are able to be hydrogenated with a much higher rate than that on the traditional catalyst under similar reaction conditions (Fig. 4f).

The H-D isotope effect was employed to further clarify the difference of IR bands on different configuration of ZrO₂/CuO-0.2 and Cu/ZrO₂-0.1 catalysts. The activated catalysts were firstly exposed to CO₂ + D₂ atmosphere for 90 min to achieve steady state (Supplementary Fig. 10), then the CO₂ supply was cut-off (Fig. 5). As shown in the Fig. 5a and c, two new bands related with deuterium exchanged D-COO* and D₃-CO* appeared at 2174 and 2056 cm⁻¹. The symmetric O-C-O vibration of formate species was observed to shift from around 1386 to 1346 cm⁻¹. The intermediate of HCOO-Cu was shifted from 1350 cm⁻¹ to

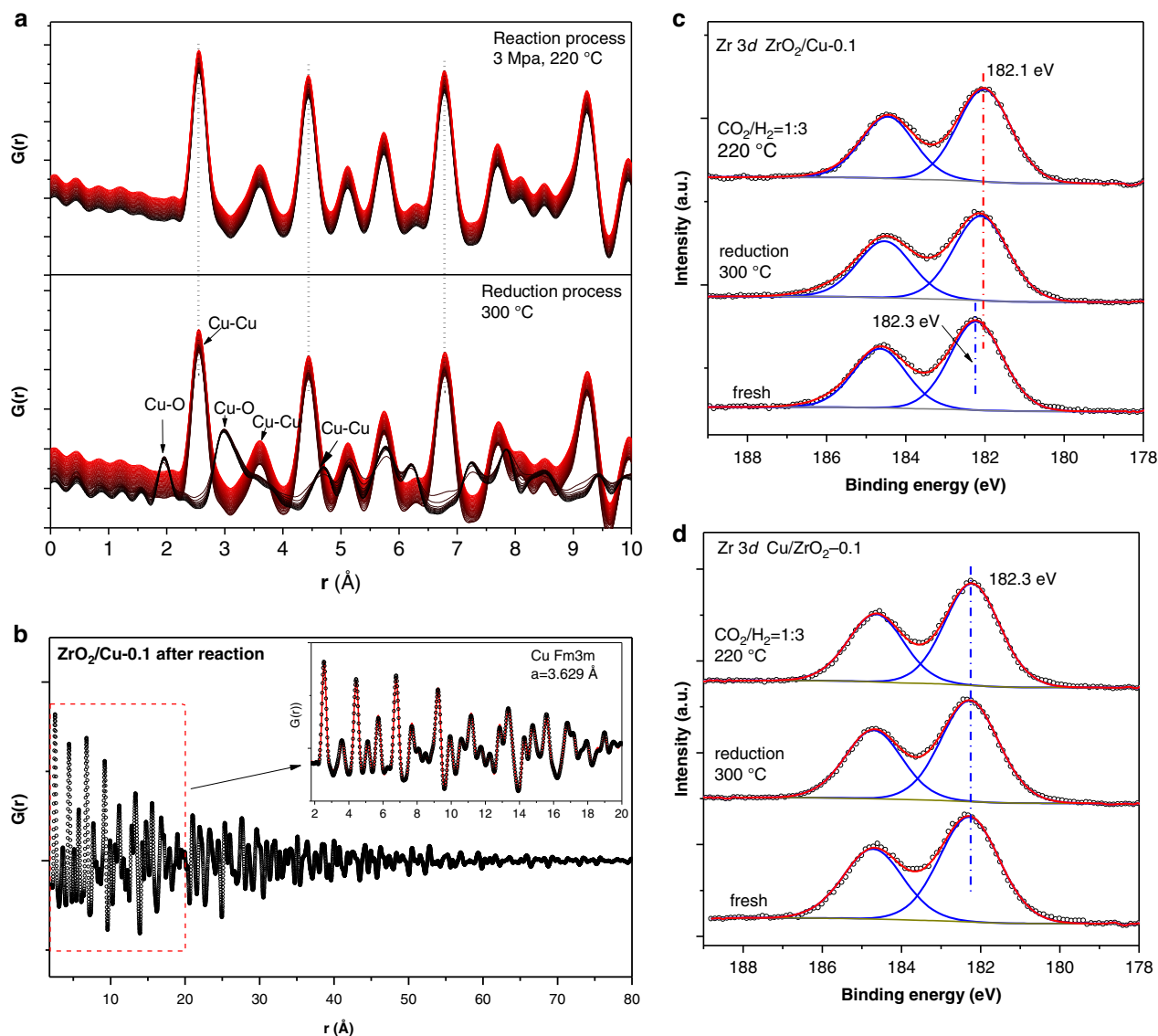
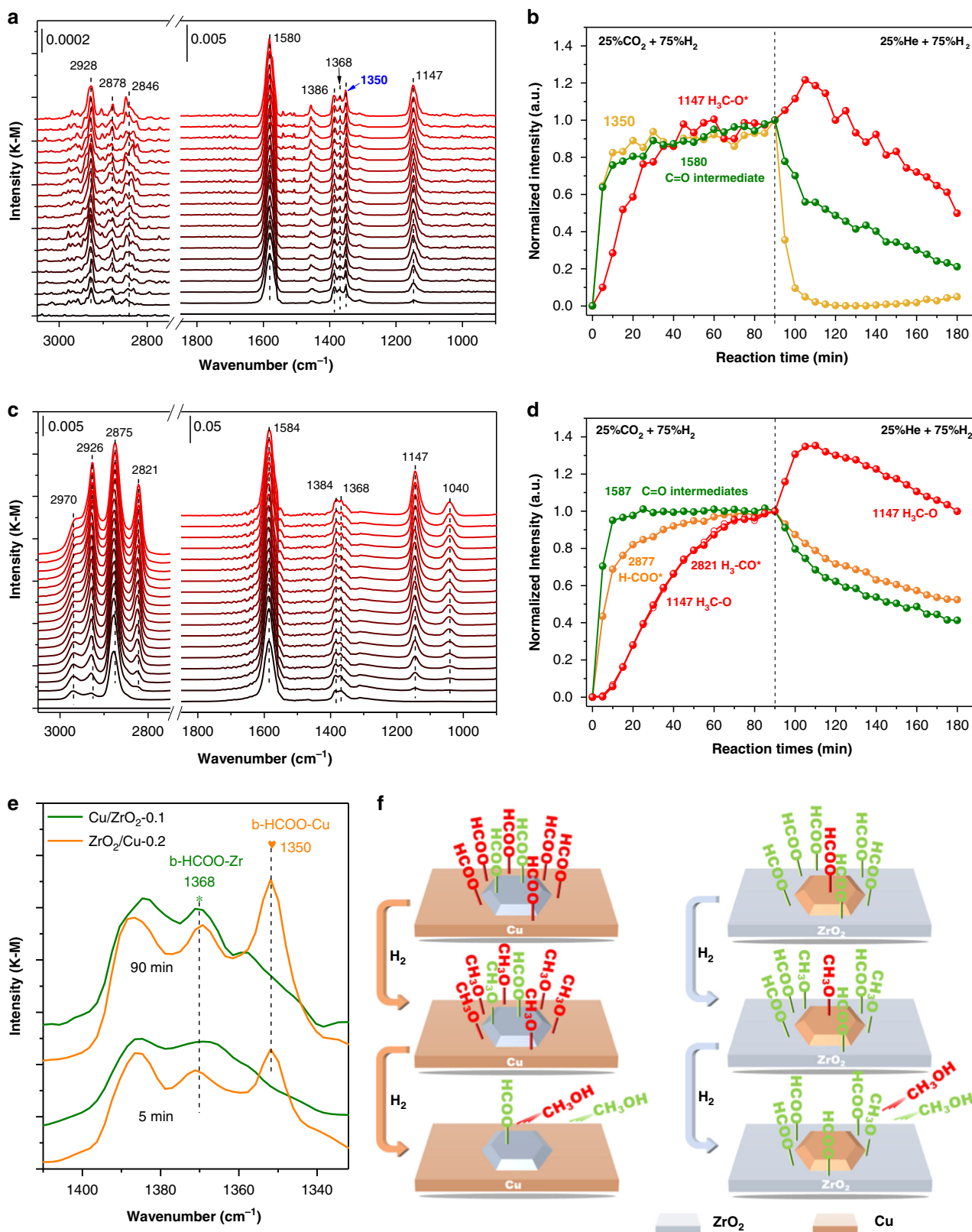


Fig. 3 In situ characterizations for the ZrO_2/Cu catalysts. **a** Pair distribution function in real space of $ZrO_2/Cu-0.1$ catalyst in reduction condition (upper panel); reduced in the flow of 5% H_2/He from room temperature to 300 °C, from black to red) and under reaction condition (bottom panel) (Reaction conditions: 2 ml min^{-1} CO_2 + 6 ml min^{-1} H_2 , 3 MPa, 220 °C, reaction time: 60 mins; from black to red). **b** The PDF and fitting profiles (inserted figure) of the post reaction $ZrO_2/Cu-0.1$ catalyst. The profile exhibited here was the last spectrum of obtained for the in situ reaction in part a. The AP-XPS Zr 3d region spectra of **c** $ZrO_2/Cu-0.1$ and **d** $Cu/ZrO_2-0.1$ catalyst.

$1323\ cm^{-1}$ of DCOO-Cu which is much clearer than in the spectra of $CO_2 + H_2$ reaction, as the previous one partially overlapped with another peak. The intensity of the DCOO-Cu over $ZrO_2/Cu-0.2$ declined within 10 min after the cut-off of the CO_2 feed (Fig. 5b). In comparison, the detectable surface species over $Cu/ZrO_2-0.1$ declined gradually in the 90 min time scale after the cut-off of CO_2 feed, while the intensity of the D_3-CO^* increases first before declining, due to the intermediate properties in the transformation from carbonates/formates to methanol (Fig. 5c, d). This comparative study of isotope effect further reveals that with the assistant of metallic Cu, the hydrogenation of the formate species (HCOO-Cu) accelerated, which probably explains the higher activity of the inverse catalyst.

Theoretical calculations on CO_2 adsorption. The in-situ IR observation has revealed that the surface adsorbates on the inverse catalyst are partially different from the traditional configuration.

Two models were used to simulate the conventional Cu/ZrO_2 and inverse ZrO_2/Cu catalysts (details seen Methods, and Supplementary Figs. 11 and 12). To obtain insight into this phenomenon, the adsorption of CO_2 on conventional Cu/ZrO_2 and inverse ZrO_2/Cu catalysts was calculated to figure out the difference of formed configurations of CO_2^* on these two surfaces (Fig. 6). The adsorption configurations of CO_2^* are essential precursors for the formation of formate species. The calculation models of Cu/ZrO_2 and inverse ZrO_2/Cu are shown in Fig. 6a, d. The adsorption free energy was obtained at a temperature of 220 °C and a pressure of 3.0 MPa to simulate real reaction conditions. Based on the results of DRIFTS, two initial adsorption modes were established on Cu/ZrO_2 and inverse ZrO_2/Cu catalysts (Fig. 6b, c, e, f), respectively. On the Cu/ZrO_2 model, the most favorable adsorption configuration of CO_2 is both of the O atoms attached to the zirconia regardless of the initial state. Two of the most representative cases are shown in Fig. 6 and the adsorption free energy are $-2.88\ eV$ or $-1.42\ eV$ respectively (Fig. 6b, c). The bonding and configuration of this kind



of CO_2^* have also been reported in previously^{41,42}. Therefore, the intermediate of COO^*-Cu is not favored to be formed on the Cu/ ZrO_2 catalyst, going well with the results of DRIFTS (Fig. 4a). On the contrary, the two different CO_2 adsorption initial states were evaluated on inverse ZrO_2/Cu surface. The adsorption of bent CO_2 at the interface (Fig. 6f) is more stable than that on ZrO_2 particle

(Fig. 6e) based on the calculated adsorption free energy (-0.27 eV vs 0.21 eV). The probability distribution of different adsorption configurations at 500 K were calculated by $P_m = \frac{1}{Z} \exp\left[\frac{-\Delta E}{k_B T}\right]$ (Supplementary Table 4). These stable adsorption configurations on Cu/ ZrO_2 and inverse ZrO_2/Cu can further convert into the formate

Fig. 4 Operando DRIFTS observation. **a, c** In situ DRIFTS spectra of the $\text{CO}_2 + \text{H}_2$ reaction on $\text{ZrO}_2/\text{Cu}-0.2$ and $\text{Cu}/\text{ZrO}_2-0.1$ catalysts. The catalysts were exposed to 75% $\text{H}_2/25\% \text{CO}_2$ (8 ml min^{-1}) atmosphere at 220°C for 90 min (black to red lines). **b, d** Normalized intensities of the typical surface species including formate (2877 cm^{-1} , orange dotted line), methoxy (2821 or 1147 cm^{-1} , red dotted line), $\text{C}=\text{O}$ ($\sim 1580 \text{ cm}^{-1}$, green dotted line) and the peak of $\text{HCOO}-\text{Cu}$ (1350 cm^{-1} , yellow dotted line) species versus reaction time (first 90 mins in 75% $\text{H}_2/25\% \text{CO}_2$ atmosphere at 220°C and the inlet was switched to 75% $\text{H}_2/25\% \text{He}$ at 90 min and maintained at the same temperature for another 90 min) over $\text{ZrO}_2/\text{Cu}-0.2$ and $\text{Cu}/\text{ZrO}_2-0.1$ catalysts. The intensities of the species were normalized to the steady state of each corresponding IR band after 90 min reaction in 75% $\text{H}_2/25\% \text{CO}_2$ atmosphere. **e** The enlarged spectra in the region of $1450-1320 \text{ cm}^{-1}$ of $\text{ZrO}_2/\text{Cu}-0.2$ (orange line) and $\text{Cu}/\text{ZrO}_2-0.1$ (green line) catalysts. **f** The scheme illustrating the reaction behaviors of the $\text{HCOO}-\text{Cu}$ and $\text{HCOO}-\text{Zr}$ intermediates on inverse ZrO_2/Cu and Cu/ZrO_2 catalysts.

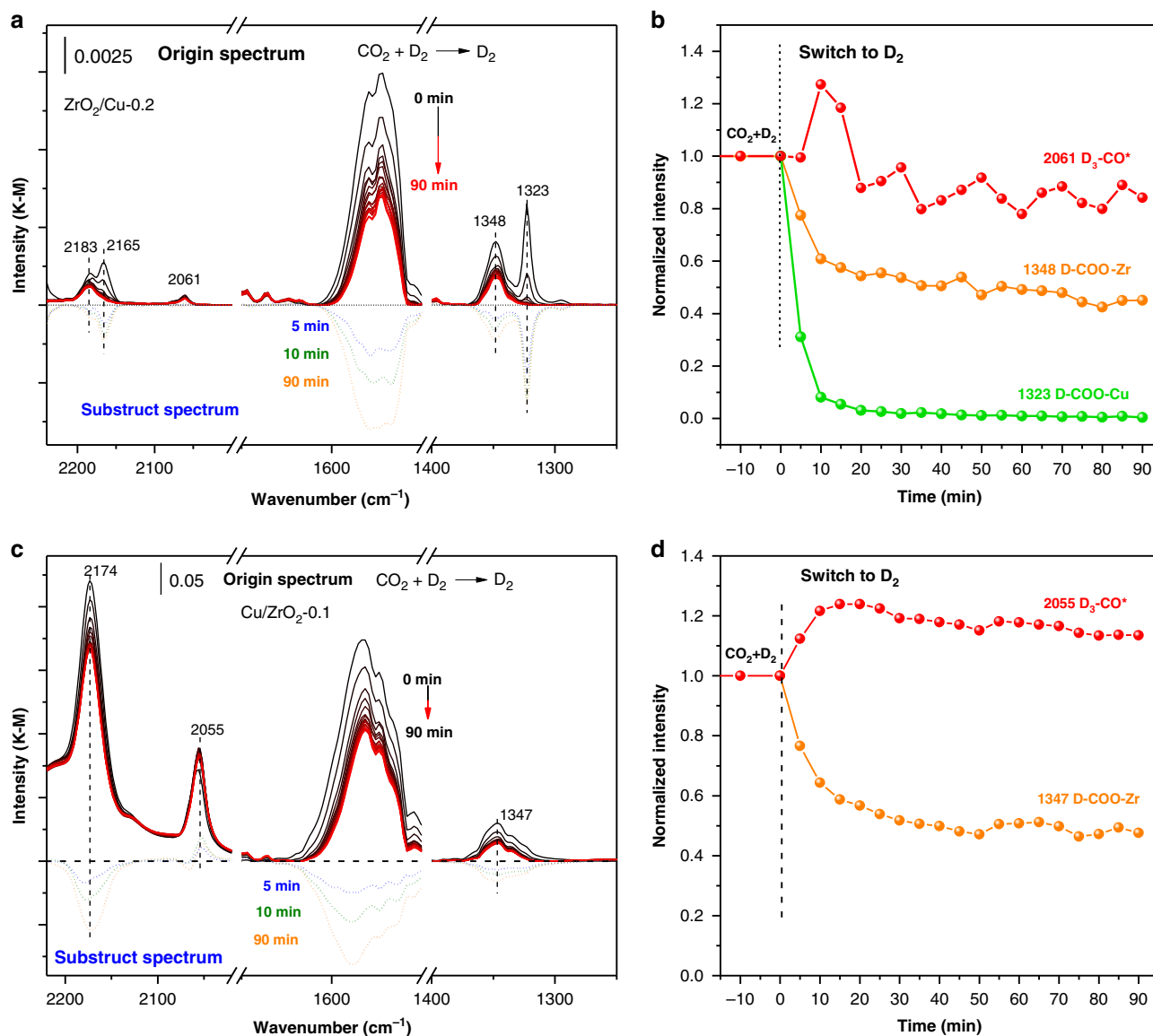


Fig. 5 In situ DRIFTS observation of surface species with isotope exchange. **a, c** In situ DRIFT spectra of surface species of the $\text{ZrO}_2/\text{CuO}-0.2$ and $\text{Cu}/\text{ZrO}_2-0.1$ catalysts in the $\text{CO}_2 + \text{D}_2$ flow and subsequently cut off the CO_2 in the D_2 flow for 90 min (the upper panel, black to red lines). The spectra in the bottom showed the spectrum at 5, 10 and 90 min differentiate spectra to the one at 0 min, 5 min (blue dash line), 10 min (green dash line), 90 min (orange dash line). **b, d** The Normalized intensity of the IR peaks of the surface formate and methoxy as a function to reaction time on $\text{ZrO}_2/\text{CuO}-0.2$ and $\text{Cu}/\text{ZrO}_2-0.1$ catalysts. The infrared intensity of the species reaching steady state at 0 min of D_2 or namely the 90 min in the $\text{CO}_2 + \text{D}_2$ flow has been arbitrarily scaled as 1 (Reaction conditions: $2 \text{ ml min}^{-1} \text{CO}_2 + \text{D}_2 \text{ ml min}^{-1} \text{H}_2$, 0.1 MPa, 493 K). D_3-CO^* (red dotted line), D-COO-Zr (orange dotted line; $\nu(\text{C-D})$: 2174 cm^{-1} , $\nu(\text{C-O})$: 1348 cm^{-1}), D-COO-Cu (green dotted line; $\nu(\text{C-O})$: 1323 cm^{-1}).

intermediate in similar chemical bonding, indicating an adsorption configuration-driven mechanism.

In summary, we have shown that an inverse ZrO_2/Cu catalyst composed of only 10% of zirconia loaded on metallic Cu particles showed a superior catalytic performance for the hydrogenation of

CO_2 to methanol when compared to a conventional zirconia supported Cu (Cu/ZrO_2) catalyst. The best ZrO_2/Cu catalyst displayed 3 times higher activity ($524 \text{ g}_{\text{MeOH}}/\text{kg}_{\text{cat}}^{-1}\text{h}^{-1}$) for the $\text{CO}_2 \rightarrow \text{CH}_3\text{OH}$ conversion. AP-XPS and DRIFTS characterizations showed that the ZrO_2 species were in a highly reduced state

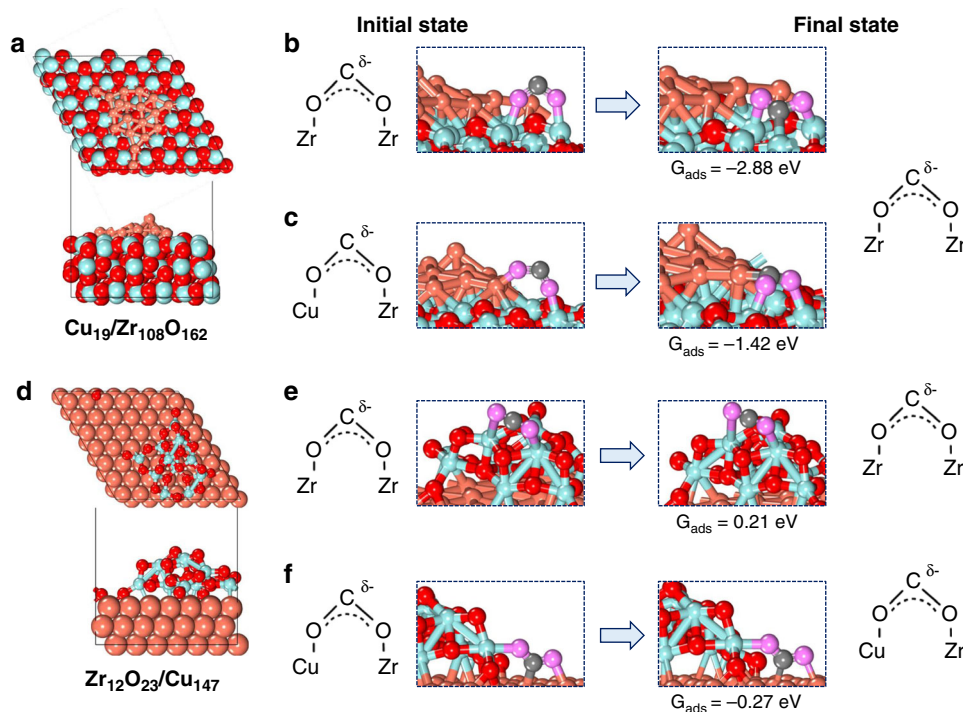


Fig. 6 The configuration and adsorption free energy of CO_2 on different models. The configurations of **a** $\text{Cu}_{19}/\text{Zr}_{108}\text{O}_{162}$ presents Cu/ZrO_2 catalyst, the initial states of CO_2 adsorbed on Cu/ZrO_2 **b** O-Zr, **c** O-Cu; the configurations of **d** $\text{Zr}_{12}\text{O}_{23}/\text{Cu}_{147}$ presents ZrO_2/Cu catalyst, the initial states of CO_2 adsorbed on inverse ZrO_2/Cu **e** O-Zr, **f** O-Cu. The salmon, cyan, black and red spheres represent Cu, Zr, C and O atoms, respectively. The pink spheres represent the O atoms in CO_2 molecule.

and intermediates of formate and methoxy were formed and consumed on the inverse ZrO_2/Cu much faster than on the Cu/ZrO_2 configuration. The high activity is mainly ascribed to the formation of a highly reactive HCOO-Cu intermediate adsorbed on the metallic Cu component of the inverse ZrO_2/Cu catalyst. The inverse configuration of ZrO_2/Cu possesses distinct structure and catalytic properties and may be extended to other practical inverse catalysts. This study illustrates the power of using an inverse oxide/metal configuration and points to a new way for designing high-performance catalysts for CO_2 hydrogenation to methanol.

Methods

Catalysts preparation. Synthesis of $\text{ZrO}_2/\text{Cu}-x$ ($x = 0.05, 0.1, 0.2, 0.5, 0.9$) catalysts. $\text{ZrO}_2/\text{Cu}-x$ catalysts were synthesized by co-precipitation method (CP). The oxalic acid was used as a precipitating agent. Taking the synthesis procedure of $\text{ZrO}_2/\text{Cu}-0.1$ catalyst as an example: 0.02 mol $\text{Cu}(\text{NO}_3)_2$ and 0.002 mol $\text{Zr}(\text{NO}_3)_4$ precursors were dissolved in 100 mL ethanol. The mixed solution of precursors was then added into 0.5 M oxalic acid in ethanol solution under vigorous stirring. After 30 min reaction, the resultant solid was separated by centrifugation, followed by washing with ethanol and drying overnight. The obtained solid was calcined in the furnace at 400°C for 2 h. The $\text{ZrO}_2/\text{Cu}-x$ catalysts with other x values were also prepared by a similar procedure. $\text{ZrO}_2/\text{Cu}-0.1\text{-NaOH}$ and $\text{ZrO}_2/\text{Cu}-0.9\text{-NaOH}$ were synthesized by using NaOH as the precipitating agent.

The loading of the Zr and Cu was determined by ICP-OES.

Catalytic evaluation. The performance evaluation for CO_2 hydrogenation to methanol was performed in a high-pressure fixed-bed flow stainless steel reactor. 50 mg catalyst was diluted with quartz sand, and then packed into the stainless-steel tubular reactor. Prior to the catalytic measurements, the catalyst was reduced in a stream of 5% H_2/N_2 at 300°C for 2 h under atmospheric pressure. Then, the temperature was cooled to 180°C , and the reductive gas was replaced by the reaction gas of CO_2 and H_2 at a ratio of 1:3 ($10\text{ ml min}^{-1}\text{ CO}_2$; $30\text{ ml min}^{-1}\text{ H}_2$). The reaction was performed with a pressure of 3.0 MPa. The catalytic activity test was taken at 180, 200 and 220°C , and each temperature hold for 3 h. The reactants and products flowing out in the reactors were analyzed by an online gas chromatographer (GC-2014, Shimadzu) equipped with a TCD and a flame ionization detector (FID). The CO_2 conversion and CH_3OH selectivity were obtained from the GC data. All the conversion at different temperature are kept below than 5%.

The conversion, selectivity and space time yield (STY) were defined in the following equation:

$$\text{Conv.}(\text{CO}_2)\% = \frac{n\text{CH}_3\text{OH} + n\text{CO} + n\text{CH}_4}{n\text{CO}_2 + n\text{CH}_3\text{OH} + n\text{CO} + n\text{CH}_4} \quad (\text{E1})$$

$$\text{Sel.}(\text{CH}_3\text{OH})\% = \frac{n\text{CH}_3\text{OH}}{n\text{CH}_3\text{OH} + n\text{CO} + n\text{CH}_4} \quad (\text{E2})$$

$$\text{STY}(\text{CH}_3\text{OH})(\text{g}_{\text{CH}_3\text{OH}} \cdot \text{kg}_{\text{cat}}^{-1} \cdot \text{h}^{-1}) = \frac{\text{FCO}_2 * \text{Conv.} * \text{Sel.}(\text{CH}_3\text{OH}) * 32 * 60}{22.4 * m_{\text{cat}}} \quad (\text{E3})$$

Structural characterization

X-ray diffraction. The ex situ XRD diffraction patterns of tested catalysts were collected at the 17 BM beamline of the Advanced Photon Source (APS), Argonne National Laboratory (ANL) using a wavelength of the incident X-ray was 0.24121 Å. The fine powder of all the samples were loaded in the Kapton tube (1.0 mm OD). The powder diffraction images were collected using a flat panel amorphous silicon detector. The diffraction patterns were integrated using GSAS-II packages from corresponding images.

The in situ XRD characterization was performed at the same beamline with the ex situ XRD. The samples were placed into the high pressure in situ Clausen cell equipped with quartz tube (1.1 mm OD and 0.2 mm wall thickness). The reduction was performed at 300°C in the flow of 5% H_2/He . While, the reaction condition was carried out at 220°C and in the presence of 3 MPa of 25% $\text{CO}_2/75\%$ H_2 mixture.

The PDF analysis of the in situ and ex situ XRD was performed using the GSAS-II packages. The composition of the samples is set based on the ICP-OES results.

X-ray adsorption fine structure. The Zr K edge and Cu K edge XAFS spectra of the catalysts were performed at BL14W beamline of the Shanghai Synchrotron Radiation Facility (SSRF) and also Beijing Synchrotron Radiation Facility (BSRF). Before the measurement, the samples were pressed into tablet.

All XAFS spectra were processed using the IFEFFIT package. The EXAFS oscillations were fitted according to back-scattering equation, using the FEFF models generated from crystal structures of ZrO_2 .

Ambient-pressure X-ray photoelectron spectroscopy. The AP-XPS measurement were carried out on a commercial SPECS AP-XPS chamber equipped with a PHOIBOS 150 EP MCD-9 analyzer (resolution: $\sim 0.4\text{ eV}$). The contaminated $\text{C}1s$ (284.6 eV) was used for the energy calibration. The $\text{ZrO}_2/\text{Cu}-0.1$, $\text{ZrO}_2/\text{Cu}-0.9$ and

amorphous CuO catalyst powders were pressed on an aluminum plate and then loaded into the AP-XPS chamber. The sample was reduced with 30 mTorr H₂ at 300 °C for 2 h and cooled down to room temperature. Then 30 mTorr of H₂ and 10 mTorr of CO₂ were introduced into the reaction chamber. Zr 3d, Cu 2p, Cu LMM, O 1s, and C 1s XPS regions were collected at different temperatures (180 °C, 200 °C, 220 °C, 240 °C) under a reaction gas environment.

Diffuse reflectance infrared fourier transform spectroscopy. Operando DRIFTS measurements were performed by using an FTIR spectrometer (Bruker Vertex 80) equipped with a Harrick cell and an MCT detector, along with an RGA detector for the outlet gas analysis. The spectra were expressed in units of Kubelka-Monk (K-M). The ZrO₂/Cu-0.2, 0.9 catalysts were reduced in 50 ml min⁻¹ (H₂ / He = 1:9) gas flow at 300 °C for 2 h and then cooled down to 220 °C. The gas flow was changed to 75% H₂/25% CO₂ (8 ml min⁻¹, 0.1 MPa) at the same temperature and the spectra were collected simultaneously. After 90 min reaction in 75% H₂/25% CO₂ atmosphere, the inlet was switched to 75% H₂/25% He (8 ml min⁻¹) at the same temperature. At the same time, DRIFTS spectra were recorded to monitor the change of intensity of different surface species for another 90 mins. The signals were normalized basing on the intensity of signals after 90 mins reaction in 75% H₂/25% CO₂ (8 ml min⁻¹) atmosphere.

TEM characterization. STEM experiments were carried out on a FEI Talos F200X electron microscope with a HAADF detector at 200 kV. EDX elemental maps were acquired from a Bruker super-X detection system on the Talos microscope.

The atomic coordination of the CuO was obtained from the Inorganic Crystal Structure Database (ICSD). Structural models and simulated electron diffraction patterns were generated by using CrystalMaker and SingleCrystal (CrystalMaker Software Ltd.).

Surface area measurement. N₂ physisorption was performed on a Micromeritics ASAP-2020 instrument. The samples were first degassed in vacuum at 200 °C for 2 h before the measurement. The specific surface area and pore size distribution were calculated by using the Brunauer-Emmett-Teller (BET) method and Barrett-Joyner-Halenda (BJH) desorption branch, respectively.

The copper surface areas were determined by N₂O titration on AutoChem II 2920 system equipped with a thermal conductivity detection (TCD) device. The samples were reduced in 5 vol% H₂-Ar flow from room temperature to 500 °C and hold for 10 min. Then the catalysts were flushed with Ar flow and the temperature was decreased to 90 °C. Next, 2 vol% N₂O in Ar was introduced to the reactor and hold for 30 min in a flow of 50 ml min⁻¹. Finally, the catalysts were cooled to room temperature under Ar flow to conduct the second TPR run. The copper metallic surface area was calculated by assuming 1.4 × 10¹⁹ copper atoms/m² and a molar stoichiometry N₂O/Cu = 0.5, where the Cus means the copper atoms on the surface.

DFT calculations

Computational models. For Cu/ZrO₂ calculation model, a Cu₁₉ cluster of truncated from Cu fcc structure was supported by a p(3 × 3) (-1 1 1) surface of monoclinic zirconia, this model contains 108 Zr, 162 O, and 19 Cu atoms as shown in Fig. 6(a), after the ab initio thermodynamics simulations of 10 ps, the Cu particle formed layered structure. During the optimization, 36 Zr and 54 O atoms were frozen while the others were relaxed. To model the inverse ZrO₂/Cu surface, three Cu atomic layers of 7 × 7 (17.898 × 17.898 Å, Fig. 6b) were used. Based on ab initio atomistic thermodynamics, the formation of one oxygen vacancy is feasible in supported Zr₁₂O₂₄ particle (Supplementary Fig. S11). Therefore, the inverse model contains 147 Cu, 12 Zr, and 23 O atoms, where 49 Cu atoms was fixed, others atoms were relaxed. In all slab models, vacuum layers of 15 Å were applied to avoid the interactions between slabs in the z-direction.

It should be noticed that the model we used in theoretical calculation is just one of the possible and representative structures of the inverse and traditional catalysts, which is used to show the influence of the configuration on the adsorption of CO₂ and support our in situ DRIFTS observation.

Computational methods. The DFT calculations were performed using the Vienna Ab Initio Simulation Package (VASP)⁴³ with the frozen-core projector-augmented wave (PAW) method⁴⁴. The generalized gradient approximation in the Perdew-Burke-Ernzerhof (GGA-PBE)⁴⁵ function including D3 correction (Becke-Jonson damping)^{46,47} was employed for the exchange-correlation energy. An onsite Coulomb correction, $U_{\text{eff}} = U - J$, of 4.0 eV, was set for Zr 4d states^{48,49}. A cutoff energy of 450 eV was selected for the plane-wave expansion. The convergence criteria for the force and electronic self-consistent iteration were set to 0.03 eV/Å and 10⁻⁵ eV, respectively. The Brillouin zone was sampled with a 1 × 1 × 1 for Cu/ZrO₂ and ZrO₂/Cu models (Supplementary Data 1 and 2). The adsorption free energy (G_{ads}) were calculated based on $G_{\text{ads}} = G_{\text{x/slab}} - [G_{\text{slab}} + G_{\text{x}}]$, where $G_{\text{x/slab}}$ is the total free energy of the slab with adsorbents after full relaxation, G_{slab} is the total free energy of the bare slab, and G_{x} is the total energy of the free adsorbents in the gas phase considering the temperature and gaseous pressure. Therefore, the more negative the G_{ads} , the stronger the adsorption. In our calculations, the effect of temperature and pressure on free energy of solid is ignored, the corrected energy for adsorbents and free gas at $T = 220$ °C and $P = 3$ MPa was obtained by

VASPKIT tool⁵⁰. Ab initio molecule dynamics (AIMD) calculations were carried out at $T = 500$ K, the canonical (NVT) ensemble was used with a time step of 1 fs during 10 ps of a well-equilibrated trajectory. The number of oxygen vacancy in inverse catalyst model was calculated based on ab initio atomistic thermodynamics, the calculation details was same as stated in previous studies⁵¹.

Data availability

The data that support the plots within this paper and other finding of this study are available from the corresponding author upon reasonable request.

Received: 8 May 2020; Accepted: 16 October 2020;

Published online: 13 November 2020

References

- Jenkinson, D. S., Adams, D. & Wild, A. Model estimates of CO₂ emissions from soil in response to global warming. *Nature* **351**, 304–306 (1991).
- Knutson, T. R. & Tuleya, R. E. Impact of CO₂-induced warming on simulated hurricane intensity and precipitation: sensitivity to the choice of climate model and convective parameterization. *J. Clim.* **17**, 3477–3495 (2004).
- Hansen, J. et al. Global temperature change. *Proc. Natl Acad. Sci. USA* **103**, 14288–14293 (2006).
- Wang, Y. et al. Rationally designing bifunctional catalysts as an efficient strategy to boost CO₂ hydrogenation producing value-added aromatics. *ACS Catal.* **9**, 895–901 (2018).
- Álvarez, A. et al. Challenges in the greener production of formates/formic acid, methanol, and DME by heterogeneously catalyzed CO₂ hydrogenation processes. *Chem. Rev.* **117**, 9804–9838 (2017).
- Kar, S., Sen, R., Goepfert, A. & Prakash, G. S. Integrative CO₂ capture and hydrogenation to methanol with reusable catalyst and amine: toward a carbon neutral methanol economy. *J. Am. Chem. Soc.* **140**, 1580–1583 (2018).
- Olah, G. A. Beyond oil and gas: the methanol economy. *Angew. Chem. Int. Ed.* **44**, 2636–2639 (2005).
- Mathew, T. George Andrew Olah (1927–2017). *Nature* **544**, 162–162 (2017).
- Goepfert, A., Olah, G. A., & Prakash, G. S. Toward a sustainable carbon cycle: the methanol economy. In *Green chemistry*, 919–962. (Elsevier, 2018).
- Lin, L. et al. Low-temperature hydrogen production from water and methanol using Pt/α-MoC catalysts. *Nature* **544**, 80–84 (2017).
- Yu, K. M. K. et al. Non-syngas direct steam reforming of methanol to hydrogen and carbon dioxide at low temperature. *Nat. Commun.* **3**, 1230 (2012).
- Tian, P., Wei, Y., Ye, M. & Liu, Z. Methanol to olefins (MTO): from fundamentals to commercialization. *ACS Catal.* **5**, 1922–1938 (2015).
- Björgen, M. et al. Conversion of methanol to hydrocarbons over zeolite H-ZSM-5: on the origin of the olefinic species. *J. Catal.* **249**, 195–207 (2007).
- Martin, O. et al. Indium oxide as a superior catalyst for methanol synthesis by CO₂ hydrogenation. *Angew. Chem. Int. Ed.* **55**, 6261–6265 (2016).
- Frei, M. S. et al. Atomic-scale engineering of indium oxide promotion by palladium for methanol production via CO₂ hydrogenation. *Nat. Commun.* **10**, 3377 (2019).
- Wang, J. et al. A highly selective and stable ZnO-ZrO₂ solid solution catalyst for CO₂ hydrogenation to methanol. *Sci. Adv.* **3**, e1701290 (2017).
- Wang, Y. et al. Exploring the ternary interactions in Cu-ZnO-ZrO₂ catalysts for efficient CO₂ hydrogenation to methanol. *Nat. Commun.* **10**, 1166 (2019).
- Rungtaweeworanit, B. et al. Copper nanocrystals encapsulated in Zr-based metal-organic frameworks for highly selective CO₂ hydrogenation to methanol. *Nano Lett.* **16**, 7645–7649 (2016).
- Studt, F. et al. The mechanism of CO and CO₂ hydrogenation to methanol over Cu-based catalysts. *ChemCatChem* **7**, 1105–1111 (2015).
- Witoon, T., Chalorntham, J., Dumrongbunditkul, P., Chareonpanich, M. & Limtrakul, J. CO₂ hydrogenation to methanol over Cu/ZrO₂ catalysts: effects of zirconia phases. *Chem. Eng. J.* **293**, 327–336 (2016).
- Kattel, S., Yan, B., Yang, Y., Chen, J. G. & Liu, P. Optimizing binding energies of key intermediates for CO₂ hydrogenation to methanol over oxide-supported copper. *J. Am. Chem. Soc.* **138**, 12440–12450 (2016).
- Bianchi, D., Gass, J.-L., Khalfallah, M. & Teichner, S. J. Intermediate species on zirconia supported methanol aerogel catalysts: I. State of the catalyst surface before and after the adsorption of hydrogen. *Appl. Catal. A Gen.* **101**, 297–315 (1993).
- Bianchi, D., Chafik, T., Khalfallah, M. & Teichner, S. J. Intermediate species on zirconia supported methanol aerogel catalysts: II. Adsorption of carbon monoxide on pure zirconia and on zirconia containing zinc oxide. *Appl. Catal. A Gen.* **105**, 223–249 (1993).
- Bianchi, D., Chafik, T., Khalfallah, M. & Teichner, S. J. Intermediate species on zirconia supported methanol aerogel catalysts: IV. adsorption of carbon dioxide. *Appl. Catal. A Gen.* **112**, 219–235 (1994).

25. Bianchi, D., Chafik, T., Khalfallah, M. & Teichner, S. J. Intermediate species on zirconia supported methanol aerogel catalysts V. adsorption of methanol. *Appl. Catal. A Gen.* **123**, 89–110 (1995).
26. Tada, S. et al. Design of interfacial sites between Cu and amorphous ZrO₂ dedicated to CO₂-to-Methanol hydrogenation. *ACS Catal.* **8**, 7809–7819 (2018).
27. Tada, S. et al. Cu species incorporated into amorphous ZrO₂ with high activity and selectivity in CO₂-to-methanol hydrogenation. *J. Phys. Chem. C.* **122**, 5430–5442 (2018).
28. Lam, E. et al. Isolated Zr surface sites on silica promote hydrogenation of CO₂ to CH₃OH in supported Cu catalysts. *J. Am. Chem. Soc.* **140**, 10530–10535 (2018).
29. Rodriguez, J. A. et al. Water-gas shift reaction on a highly active inverse CeOx/Cu (111) catalyst: unique role of ceria nanoparticles. *Angew. Chem. Int. Ed.* **48**, 8047–8050 (2009).
30. Senanayake, S. D., Stacchiola, D. & Rodriguez, J. A. Unique properties of ceria nanoparticles supported on metals: novel inverse ceria/copper catalysts for CO oxidation and the water-gas shift reaction. *Acc. Chem. Res.* **46**, 1702–1711 (2013).
31. Lunkenbein, T., Schumann, J., Behrens, M., Schlögl, R. & Willinger, M. G. Formation of a ZnO overlayer in industrial Cu/ZnO/Al₂O₃ catalysts induced by strong metal-support interactions. *Angew. Chem. Int. Ed.* **54**, 4544–4548 (2015).
32. Schumann, J. et al. Promoting strong metal support interaction: doping ZnO for enhanced activity of Cu/ZnO: M (M= Al, Ga, Mg) catalysts. *ACS Catal.* **5**, 3260–3270 (2015).
33. Rodriguez, J. A. et al. Hydrogenation of CO₂ to methanol: importance of metal-oxide and metal-carbide interfaces in the activation of CO₂. *ACS Catal.* **5**, 6696–6706 (2015).
34. Gadkari, A., Shinde, T. & Vasambekar, P. Structural analysis of Y³⁺-doped Mg-Cd ferrites prepared by oxalate co-precipitation method. *Mater. Chem. Phys.* **114**, 505–510 (2009).
35. Lemaux, S., Bensaddik, A., Van der Eerden, A., Bitter, J. & Koningsberger, D. Understanding of enhanced oxygen storage capacity in Ce_{0.5}Zr_{0.5}O₂: the presence of an anharmonic pair distribution function in the ZrO₂ subshell as analyzed by XAFS spectroscopy. *J. Phys. Chem. B* **105**, 4810–4815 (2001).
36. Zuo, J.-M., Vartanyants, L., Gao, M., Zhang, R. & Nagahara, L. Atomic resolution imaging of a carbon nanotube from diffraction intensities. *Science* **300**, 1419–1421 (2003).
37. Morant, C., Sanz, J., Galan, L., Soriano, L. & Rueda, F. An XPS study of the interaction of oxygen with zirconium. *Surf. Sci.* **218**, 331–345 (1989).
38. Lin, L. et al. In situ characterization of Cu/CeO₂ nanocatalysts for CO₂ hydrogenation: morphological effects of nanostructured ceria on the catalytic activity. *J. Phys. Chem. C.* **122**, 12934–12943 (2018).
39. Jung, K.-D. & Bell, A. T. Role of hydrogen spillover in methanol synthesis over Cu/ZrO₂. *J. Catal.* **193**, 207–223 (2000).
40. Fisher, I. A. & Bell, A. T. In-situ infrared study of methanol synthesis from H₂/CO₂ over Cu/SiO₂ and Cu/ZrO₂/SiO₂. *J. Catal.* **172**, 222–237 (1997).
41. Larmier, K. et al. CO₂-to-methanol hydrogenation on zirconia-supported copper nanoparticles: reaction intermediates and the role of the metal-support interface. *Angew. Chem. Int. Ed.* **56**, 2318–2323 (2017).
42. Silaghi, M.-C., Comas-Vives, A. & Coperet, C. CO₂ Activation on Ni/γ-Al₂O₃ catalysts by first-principles calculations: from ideal surfaces to supported nanoparticles. *ACS Catal.* **6**, 4501–4505 (2016).
43. Kresse, G. & Furthmüller, J. Efficient iterative schemes for ab initio total-energy calculations using a plane-wave basis set. *Phys. Rev. B* **54**, 11169–11186 (1996).
44. Blöchl, P. E. Projector augmented-wave method. *Phys. Rev. B* **50**, 17953–17979 (1994).
45. John, P. & Perdew, K. B. Matthias Ernzerhof. Generalized gradient approximation made simple. *Phys. Rev. Lett.* **77**, 3865–3868 (1996).
46. Grimme, S., Antony, J., Ehrlich, S. & Krieg, H. A consistent and accurate ab initio parametrization of density functional dispersion correction (DFT-D) for the 94 elements H-Pu. *J. Chem. Phys.* **132**, 154104 (2010).
47. Grimme, S., Ehrlich, S. & Goerigk, L. Effect of the damping function in dispersion corrected density functional theory. *J. Comput. Chem.* **32**, 1456–1465 (2011).
48. Puigdollers, A. & Pacchioni, G. Reducibility of ZrO₂/Pt₃Zr and ZrO₂/Pt 2D films compared to bulk zirconia: a DFT+U study of oxygen removal and H₂ adsorption. *Nanoscale* **9**, 6866–6876 (2017).
49. Puigdollers, A., Illas, F. & Pacchioni, F. Structure and properties of zirconia nanoparticles from density functional theory calculations. *J. Phys. Chem. C.* **120**, 4392–4402 (2016).
50. Wang, V., Xu, N., Liu, J.-C., Tang, G. & Geng, W. T. VASPKIT: a pre- and post-processing program for VASP code. Preprint at <https://arxiv.org/abs/1908.08269> (2019).
51. Meng, Y. et al. When density functional approximations meet iron oxides. *J. Chem. Theory Comput.* **12**, 5132–5144 (2016).

Acknowledgements

This work was financially supported by the Natural Science Foundation of China (21725301, 91645115, 21821004, 21932002, 21473229, 91545121), the National Key R&D Program of China (2017YFB0602200) and Beijing National Laboratory for Molecular Science (BNLM202011). XAS experiments were conducted at the Shanghai Synchrotron Radiation Facility (SSRF) and Beijing Synchrotron Radiation Facility (BSRF). The experiments of DRIFTS and AP-XPS carried out at the Chemistry Department of Brookhaven National Laboratory (BNL) were supported by the division of Chemical Science, Geoscience, and Bioscience, Office of Basic Energy Science of the U.S. Department of Energy (DOE) under contract No. DE-SC0012704. Use of the Advanced Photon Source (beamlines 17-BM, for XRD-PDF characterization) was supported by the U.S. DOE under contract no. DE-AC02-06CH11357. The authors are also grateful for funding support from Synfuels China, Co. Ltd. We also acknowledge the innovation foundation of Institute of Coal Chemistry, Chinese Academy of Sciences, Hundred-Talent Program of Chinese Academy of Sciences, Shanxi Hundred-Talent Program and National Thousand Young Talents Program of China. Young Elite Scientist Sponsorship Program by CAST, NO. 2019QNRC001 is also acknowledged.

Author contributions

D.M. and J.R. designed the study. C.W., J.Z. and B.Y. performed most of the reactions. L.L. carried out the AP-XPS, in situ XRD-PDF and DRIFTS analysis. W. X. did the fitting analysis for the in situ XRD-PDF characterization. J.Li and X.W. did the DFT calculation. F.Z. and W.X. did the in situ XRD-PDF measurement at APS. N.R. did the AP-XPS measurement. Y.D. and Y.Z. did the XAFS characterization. T.Z., F.Y., and J. Lu carried out the measurement and analysis of EM images. L.L., S.Y., C.W., J.R. and D.M. wrote the paper. All authors performed certain experiments, discussed and revised the paper.

Competing interests

The authors declare no competing interests.

Additional information


Supplementary information is available for this paper at <https://doi.org/10.1038/s41467-020-19634-8>.

Correspondence and requests for materials should be addressed to L.L., X.-D.W., J.A.R. or D.M.

Peer review information *Nature Communications* thanks the anonymous reviewer(s) for their contribution to the peer review of this work.

Reprints and permission information is available at <http://www.nature.com/reprints>

Publisher's note Springer Nature remains neutral with regard to jurisdictional claims in published maps and institutional affiliations.

 **Open Access** This article is licensed under a Creative Commons Attribution 4.0 International License, which permits use, sharing, adaptation, distribution and reproduction in any medium or format, as long as you give appropriate credit to the original author(s) and the source, provide a link to the Creative Commons license, and indicate if changes were made. The images or other third party material in this article are included in the article's Creative Commons license, unless indicated otherwise in a credit line to the material. If material is not included in the article's Creative Commons license and your intended use is not permitted by statutory regulation or exceeds the permitted use, you will need to obtain permission directly from the copyright holder. To view a copy of this license, visit <http://creativecommons.org/licenses/by/4.0/>.

© The Author(s) 2020